11th ANKARA INTERNATIONAL AEROSPACE CONFERENCE **AIAC-2021-001**
8-10 September 2021 - METU, Ankara TURKEY

SIMULATION OF HYPERSONIC SHOCK WAVE LAMINAR BOUNDARY LAYER INTERACTIONS

Doyle Knight* and Nadia Kianvashrad†
and Mehrnaz Rouhi Youssefi‡
Rutgers, The State University of New Jersey
New Brunswick, New Jersey USA 08903

ABSTRACT

Recent interest in hypersonic flight has refocused attention on the accuracy of non-equilibrium models for hypersonic shock wave laminar boundary layer interaction. A recent set of experiments performed at the CALSPAN University of Buffalo Research Center (CUBRC) for two configurations has been examined to assess its suitability for evaluation of non-equilibrium simulation models. Experimental data include surface heat transfer and surface pressure. Results indicate that the experimental data do not provide a stringent test of non-equilibrium effects, but rather the experimental data is best modeled by a thermal equilibrium model.

INTRODUCTION

The resurgence of interest in hypersonics during the past two decades is evident worldwide. Examples of research flight tests include the Hypersonic International Flight Research Experimentation (HIFiRE) program of the Australian Department of Defense and United States Air Force Flight Dynamics Laboratory (Jackson et al. [2015]), the Chinese DF-ZF Hypersonic Glide Vehicle (HGV) (Perrett et al. [2014]), the Scramjet Powered Accelerator for Reusable Technology Advancement (SPARTAN) at the University of Queensland (Button [2016]), the SHarp Edge Flight Experiment (SHEFEX) at the Deutsches Zentrum für Luft-und Raumfahrt (DLR) (Longo [2009]), the HEXAFLY (Steelant et al. [2015]) and HEXAFLY-INT (Pezzella et al. [2015]) experimental flight test vehicles, and the United States Defense Advanced Research Projects Agency (DARPA) Force Application and Launch from CONtinental United States (FALCON) project (Walker and Rodgers [2005]). Commercial launch vehicles include SpaceX Dragon and Starship, Blue Origin New Shepard and New Glenn, and the Boeing Starliner Spacecraft.

The aerothermodynamic loads (i.e., surface heat transfer, pressure and skin friction) on hypersonic vehicles are strongly affected by the interaction of shock waves with the vehicle boundary layer. An example is the US Space Shuttle flight STS-1. During reentry, the body flap was commanded to a maximum deflection of 14° in order to maintain pitch stability, far exceeding the planned deflection of

---

[*] Professor, Department of Mechanical and Aerospace Engineering, Email: doyleknight@gmail.com

[†] Postdoctoral Associate, Department of Mechanical and Aerospace Engineering, Email: nadiakianvashrad@gmail.com

[‡] PhD, Department of Mechanical and Aerospace Engineering, Email: mehrnazrouhi@gmail.com

8° to 9° (Maus et al. [1984]; Aeronautics and Administration [2003]). Subsequent detailed analysis indicated that the CFD predictions for the pressure distribution associated with the shock wave boundary layer interaction on the underside of the vehicle were in error at hypersonic speeds.

Hypersonic shock wave boundary layer interactions can be categorized as 1) purely laminar, 2) transitional (i.e., the boundary layer transitioning from laminar to turbulent ahead of or within the shock wave boundary layer interaction), and 3) fully turbulent. The fluid physics can be quite complex due to non-equilibrium effects including vibrational-translational energy exchange, thermochemical reactions, radiation and gas-surface interactions. Significant research efforts have focused on many of these aspects. A recent review is Babinsky and Harvey [2011].

A fundamental question is "What is the capability for accurate prediction of aerothermodynamic loading in hypersonic shock wave boundary layer interactions ?" In this regards, "accurate prediction" implies the prediction of aerothermodynamic loading within experimental uncertainty. A recent survey by Knight and Mortazavi [2018] addressed this question for shock wave laminar boundary layer interactions. A total of seventy CFD simulations of shock wave laminar boundary layer interactions were evaluated, comprising the specific geometries of a double cone and hollow cylinder flare. The authors concluded that there is no consistent accurate prediction of aerothermodynamic loading in hypersonic shock wave laminar boundary layer interactions.

A recent series of experiments were conducted at the CALSPAN University of Buffalo Research Center (CUBRC) on hypersonic shock wave laminar boundary layer interactions (see below). These experiments were performed in the LENS XX expansion tunnel for double cone and hollow cylinder flare configurations, and covered a range of Mach numbers from 10.9 to 13.2 and stagnation enthalpies from 5.44 MJ/kg to 21.85 MJ/kg. The experiments were part of a "blind" study of CFD models for hypersonic shock wave laminar boundary layer interactions which were presented at the AIAA AVIATION 2014 meeting (MacLean et al. [2014a,b]). The experimental freestream conditions are well understood since LENS XX is an expansion tunnel (MacLean et al. [2014a]) and thus uncertainties associated with vibrational freezing in shock tunnels are not present (Knight and Mortazavi [2018]). These CUBRC experiments have emerged as a favorite test for assessment of CFD modeling based upon the expectation that the high stagnation enthalpies would result in significant non-equilibrium effects in the measured aerothermodynamic loading (i.e., surface heat transfer and pressure).

The objective of this paper is to summarize our CFD simulations of the CUBRC experiments, and to answer the question "Do these CUBRC experiments constitute a stringent test of non-equilibrium effect in CFD modeling ?"

EXPERIMENTS

A series of experiments were performed at the CALSPAN University of Buffalo Research Center (CUBRC) for a double cone (Fig. 1) and hollow cylinder flare (Fig. 2). The experiments were performed in the CUBRC LENS XX tunnel. A description of the LENS XX facility is provided in Dufrene et al. [2010, 2011].

Double Cone

The double cone (Fig. 1) comprises a 25° forward cone and 55° aft cone. The overall length is 194 mm. A total of six runs were performed at CUBRC. The flow conditions are listed in Table 1. Experimental diagnostics include 23 pressure transducers and 49 heat transfer gauges. Run Nos. 1, 2, 4 and 6 were computed as described in METHODOLOGY and shown in **boldface**. The Reynolds number based upon the freestream conditions and running length of the forward cone ranged from 23,507 to 42,672 thereby assuring a fully laminar flow as indicated by MacLean et al. [2014a]. The gas is air in full chemical and thermochemical equilibrium with mass fractions of N_2 and O_2 equal to 0.765 and 0.235, respectively. The surface of the model is isothermal at 300 K.

Hollow Cylinder Flare

The hollow cylinder flare (Fig. 2) comprises a hollow cylinder with length 101.6 mm affixed to a 30° conical flare. A total of five runs were performed at CUBRC. The flow conditions are listed in Table 2. Experimental diagnostics include 18 pressure transducers and 51 heat transfer gauges. Run Nos. 1, 2, 4 and 5 were computed as describec in METHODOLOGY and shown in **boldface**. The Reynolds number based upon the length of the cylinder ranged from 12,192 to 42,672 thereby assuring a fully laminar flow as indicate by MacLean et al. [2014a]. The gas is air in full chemical and thermochemical equilibrium with mas fractions of N_2 and O_2 equal to 0.765 and 0.235, respectively. The surface of the model is isothermal at 300 K.

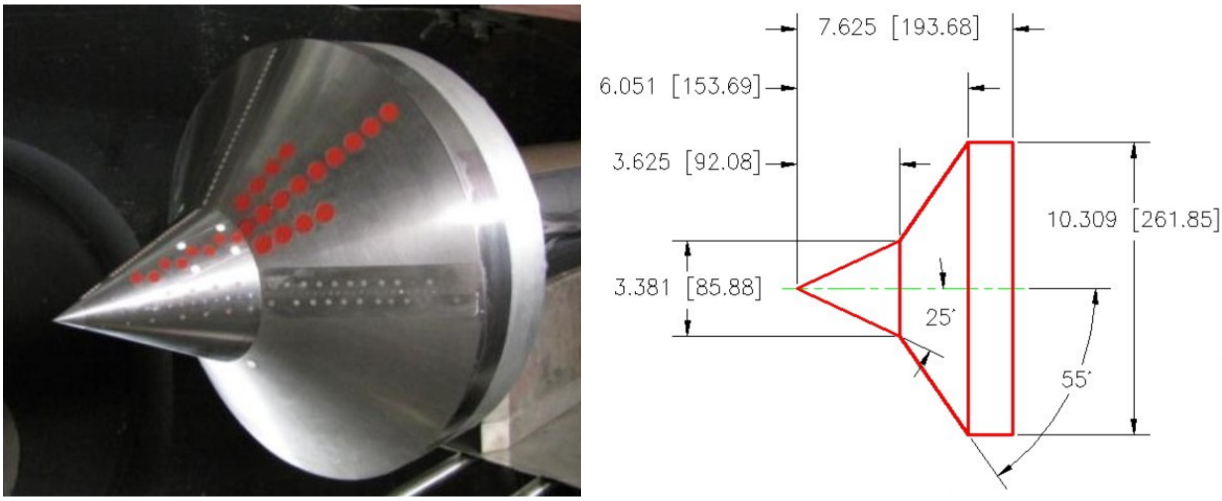

(a) Photo (b) Drawing

Figure 1: Double cone. Dimensions in inches [mm].

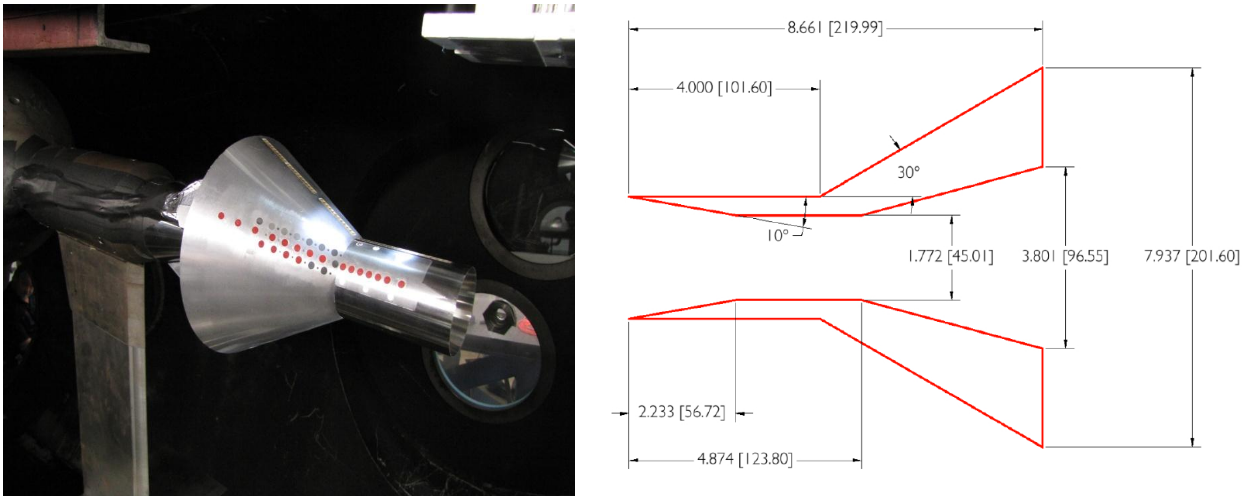

(a) Photo (b) Drawing

Figure 2: Hollow cylinder flare. Dimensions in inches [mm].

Table 1: Flow Conditions - Double Cone

Run No.	Total Enthalpy (MJ/kg)	Mach Number	Pitot Pressure (kPa)	Unit Reynolds ($/10^6$ m^{-1})	Velocity (km/s)	Density (gm/m^3)	Temperature (K)
1	**5.44**	**12.2**	**5.1**	**0.14**	**3.246**	**0.499**	**175**
2	**9.65**	**10.9**	**17.5**	**0.19**	**4.303**	**0.984**	**389**
3	18.70	13.23	18.0	0.11	6.028	0.510	521
4	**21.77**	**12.82**	**39.5**	**0.20**	**6.497**	**0.964**	**652**
5	18.51	13.14	36.8	0.23	5.996	1.057	523
6	**15.23**	**11.46**	**59.0**	**0.39**	**5.466**	**2.045**	**573**

Table 2: Flow Conditions - Hollow Cylinder Flare

Run No.	Total Enthalpy (MJ/kg)	Mach Number	Pitot Pressure (kPa)	Unit Reynolds ($/10^6$ m^{-1})	Velocity (km/s)	Density (gm/m^3)	Temperature (K)
1	**5.07**	**11.3**	**5.9**	**0.15**	**3.123**	**0.634**	**189**
2	**10.43**	**12.6**	**9.7**	**0.12**	**4.497**	**0.499**	**318**
3	11.25	11.9	36.5	0.37	4.660	1.750	383
4	**15.54**	**11.5**	**64.0**	**0.42**	**5.470**	**2.216**	**569**
5	**21.85**	**13.2**	**39.0**	**0.20**	**6.515**	**0.947**	**618**

METHODOLOGY

The overall governing equations are the laminar Navier-Stokes equations for thermally perfect non-equilibrium compressible viscous flow. A reacting mixture of gases with density ρ_α for $\alpha = 1, \ldots, n$ of which $\alpha = 1, \ldots, m$ constitute diatomic (or polyatomic) species and the remainder ($i = m{+}1, \ldots, n$) represent monatomic species are considered.

Several versions of the governing equations were considered in order to assess the extent of non-equilibrium effects as described later.

Conservation of Mass

The conservation of mass is

$$\frac{\partial \rho_\alpha}{\partial t} + \frac{\partial \rho_\alpha u_j}{\partial x_j} = \dot{\omega}_\alpha^{\mathrm{spe}} + \frac{\partial}{\partial x_j}\left[\rho D \frac{\partial Y_\alpha}{\partial x_j}\right] \quad \text{for } \alpha = 1, \ldots, n \tag{1}$$

where ρ_α is the density of species α, the mass-averaged velocity is u_j, and ρ is the mixture density $\rho = \sum_{\alpha=1}^{N} \rho_\alpha$ and the mass fraction is defined as $Y_\alpha = \frac{\rho_\alpha}{\rho}$.
The rate of production of species α is denoted as $\dot{\omega}_\alpha^{\mathrm{spe}}$ and defined as

$$\dot{\omega}_\alpha^{\mathrm{spe}} = \mathcal{M}_\alpha \sum_{j=1}^{J} \left(\nu''_{\alpha,j} - \nu'_{\alpha,j}\right) k_{f,j} \left[\prod_{l=1}^{n} \left(\frac{\rho_l}{\mathcal{M}_l}\right)^{\nu'_{l,j}} - \frac{1}{k_{e,j}} \prod_{l=1}^{n} \left(\frac{\rho_l}{\mathcal{M}_l}\right)^{\nu''_{l,j}}\right] \quad \text{for } \alpha = 1, \ldots, n \tag{2}$$

for the general reaction expressions

$$\nu'_{1,j} X_1 + \ldots + \nu'_{n,j} X_n \rightleftharpoons \nu''_{1,j} X_1 + \ldots + \nu''_{n,j} X_n \quad \text{for } j = 1, \ldots, J \tag{3}$$

where J is the number of reactions, and $\nu'_{\alpha,j}$ and $\nu''_{\alpha,j}$ are the stoichiometric coefficients of the reactants and products X_α in the j^{th} reaction.

The diffusion of species is modeled by Fick's Law assuming a uniform diffusivity D defined by $D = \frac{k}{\rho c_{p_f} Le}$, where $Le = 1.0$ is the constant Lewis number, k is the mixture thermal conductivity, and c_{p_f} is the mixture specific heat at constant pressure defined by $c_{p_f} = \sum_{\alpha=1}^{n} Y_\alpha \, c_{p_\alpha}$.

Conservation of Momentum

The conservation of momentum is

$$\frac{\partial \rho u_i}{\partial t} + \frac{\partial \rho u_i u_j}{\partial x_j} = -\frac{\partial p}{\partial x_i} + \frac{\partial \tau_{ij}}{\partial x_j} \quad \text{for } i = 1, 2, 3 \tag{4}$$

where τ_{ij} is the laminar viscous stress tensor defined as

$$\tau_{ij} = -\frac{2}{3}\mu \frac{\partial u_k}{\partial x_k}\delta_{ij} + \mu \left(\frac{\partial u_i}{\partial x_j} + \frac{\partial u_j}{\partial x_i} \right) \tag{5}$$

Conservation of Total Energy

The total energy per unit mass ε is the sum of the internal energy per unit mass e and the kinetic energy per unit mass, $\varepsilon = e + \frac{1}{2} u_j u_j$. The internal energy per unit mass e is the sum of the internal energies of each of the n species, $e = \sum_{\alpha=1}^{n} Y_\alpha \, e_\alpha$, where the internal energy per unit mass of each species e_α is the sum of an equilibrium internal energy $e_\alpha^{\text{eq}}(T)$ due to random translational energy and rotational energy (in the case of molecules) at a bulk equilibrium temperature T and a non-equilibrium internal energy $e_\alpha^{\text{vib}}(T_\alpha^{\text{vib}})$ due to vibrational excitation (in the case of molecules), $e_\alpha = e_\alpha^{\text{eq}}\,(T) + e_\alpha^{\text{vib}}(T_\alpha^{\text{vib}})$. The equilibrium internal energy of species α is

$$e_\alpha^{\text{eq}}(T) = h_{f_\alpha}^o + \int_{T_{\text{ref}}}^{T} c_{v_\alpha}(T)\, dT \tag{6}$$

The conservation of total energy is

$$\frac{\partial \rho \varepsilon}{\partial t} + \frac{\partial}{\partial x_j} \left(\rho \varepsilon + p \right) u_j = -\frac{\partial q_j}{\partial x_j} + \frac{\partial \tau_{ij} u_i}{\partial x_j} \tag{7}$$

where the heat transfer vector is defined by

$$q_j = -k \frac{\partial T}{\partial x_j} - \sum_{\alpha=1}^{m} k_\alpha^{\text{vib}} \frac{\partial T_\alpha^{\text{vib}}}{\partial x_j} - \sum_{\alpha=1}^{n} \rho h_\alpha D \frac{\partial Y_\alpha}{\partial x_j} \tag{8}$$

The static enthalpy per unit mass for species α is

$$h_\alpha = h_{f_\alpha}^o + \int_{T_{\text{ref}}}^{T} c_{p_\alpha}(T)\, dT \tag{9}$$

where $h_{f_\alpha}^o$ is the enthalpy of formation of species α at T_{ref}.

Conservation of Vibrational Energy

The conservation of vibrational energy is

$$\frac{\partial \rho_\alpha e_\alpha^{\text{vib}}}{\partial t} + \frac{\partial \rho_\alpha e_\alpha^{\text{vib}} u_j}{\partial x_j} = -\frac{\partial q_{\alpha_j}^{\text{vib}}}{\partial x_j} + \dot{\omega}_\alpha^{\text{vib}} \quad \text{for } \alpha = 1, \ldots, m \tag{10}$$

The heat transfer vector is

$$q_{\alpha_j}^{\text{vib}} = -k_\alpha^{\text{vib}} \frac{\partial T_\alpha^{\text{vib}}}{\partial x_j} - \rho D e_\alpha^{\text{vib}} \frac{\partial Y_\alpha}{\partial x_j} \tag{11}$$

The source term which does not include the vibrational-vibrational energy transfer is

$$\dot{\omega}_\alpha^{\text{vib}} = \rho_\alpha \dot{e}_\alpha^{\text{vib}} + \dot{\omega}_\alpha^{\text{spe}} e_\alpha^{\text{vib}} \tag{12}$$

where $\dot{e}_\alpha^{\text{vib}}$ is the translational-vibrational energy transfer per unit mass of species α. We consider the classical Landau-Teller model (Vincenti and Kruger [1965])

$$\dot{e}_\alpha^{\text{vib}} = \frac{e_\alpha^{\text{vib}^*}(T) - e_\alpha^{\text{vib}}(T_\alpha^{\text{vib}})}{\tau_\alpha} \tag{13}$$

where $e_\alpha^{\text{vib}^*}$ is the equilibrium vibrational energy per unit mass of species α defined by

$$e_\alpha^{\text{vib}^*}(T) = \frac{R_\alpha \Theta_\alpha^{\text{vib}}}{\exp(\Theta_\alpha^{\text{vib}}/T) - 1} \tag{14}$$

and τ_α is the relaxation time (Millikan and White [1963]) of species α.

In the second term in Eq. (12), there are two possible choices for e_α^{vib} namely, $e_\alpha^{\text{vib}} = \frac{R_\alpha \Theta_\alpha^{\text{vib}}}{\exp(\Theta_\alpha^{\text{vib}}/T)-1}$ and $e_\alpha^{\text{vib}} = \frac{R_\alpha \Theta_\alpha^{\text{vib}}}{\exp(\Theta_\alpha^{\text{vib}}/T_\alpha^{\text{vib}})-1}$. For all cases presented here, the former method is used.

Equation of State

The equation of state is $p = T\sum_{\alpha=1}^{n} \rho_\alpha R_\alpha$, where the gas constant R_α for species α is $R_\alpha = \frac{\mathcal{R}}{\mathcal{M}_\alpha}$, where $\mathcal{R}$ is the Universal Gas Constant.

Thermodynamic Data and Transport Properties

The species thermodynamic data and species transport properties are obtained from Gupta, Yos, Thompson and Lee (Gupta et al. [1990]) (NASA-RP-1232) database. The mixture viscosity μ and thermal conductivity k are determined by Wilke's Rule (Wilke [1950]). The vibrational thermal conductivity of species α is $k_\alpha^{\text{vib}} = \mu_\alpha R_\alpha$, where μ_α and R_α are the molecular viscosity and gas constant for species α, respectively.

Thermochemistry Model

The non-equilibrium Navier-Stokes simulations used the Park I thermochemistry model (Park [1985]) comprising five species (N_2, O_2, NO, N, O) and seventeen reactions (see APPENDIX).

Simulation Models

The assessment of the importance of non-equilibrium effects in prediction of the aerothermodynamic loading (i.e., surface heat transfer and pressure) for the CUBRC experiments was performed in a rational manner. The simplest model is **Perfect Gas** which assumes constant specific heats and equilibrium flow (i.e., no thermochemical reactions or vibrational-translational energy exchange). The next model is **Thermally Perfect** which incorporates temperature dependent specific heats but otherwise assumes equilibrium flow. The third model is **Non-Reactive** which adds vibrational-translational energy exchange to the previous model but omits thermochemical reactions. The final model is **Park I** incorporating both vibrational-translational energy exchange and thermochemical reactions, together with temperature dependent specific heats.

Table 3: Model Specifications

Model	Modifications		Transport properties			
	$\dot{\omega}_\alpha^{\text{spe}}$	$\dot{\omega}_\alpha^{\text{vib}}$	Specific heat	Viscosity	Pr_∞	Le
Perfect Gas	0	0	constant	Sutherland	0.72	n/a
Thermally Perfect	0	0	GW	GW	0.73652	1.0
Non-Reactive	0	$\rho_\alpha \dot{e}_\alpha^{\text{vib}}$	GW	GW	0.73607	1.0
Park I	Eq. (2) and Park I	Eq. (12)	GW	GW	0.73652	1.0

GW Gupta et al database (Gupta et al. [1990]) and Wilke's Rule (Wilke [1950])

Details of Simulations

The present paper summarizes the results of our simulations of the double cone and hollow cylinder flare models for the cases indicated in **boldface** in Tables 1 and 2. Simulations were performed using the commercial codes GASPex and GASP (Neel and McGrory [2014]) and the non-equilibrium compressible Navier-Stokes code developed in our laboratory. Details are presented in Kianvashrad and Knight, Youseffi and Knight [2015], Kianvashrad and Knight [2016], Youssefi and Knight [2016], Kianvashrad and Knight [2017a], Kianvashrad and Knight [2017b], Kianvashrad and Knight [2017c], Youssefi and Knight [2017], Kianvashrad and Knight [2018], Knight and Kianvashrad [2018] and Kianvashrad and Knight [2019].

RESULTS

Double Cone

The flowfield structure for the double cone is illustrated in Fig. 3. Contours of Mach number (Fig. 3 (a)) and static pressure (Fig. 3 (b)) are shown for Run 1 using the Perfect Gas model. The basic features are typical for all of the simulations. The forward cone generates an attached shock wave. The aft cone generates a second shock wave (bow shock) resulting in an adverse pressure gradient in the vicinity of the intersection of the forward and aft cones. The laminar boundary layer separates to form an axisymmetric recirculation region and a consequent separation shock. The forward shock and separation shock intersect upstream of the separation location. The resultant shock intersects the bow shock forming a triple point. The reattachment of the boundary layer generates a reattachment shock which intersects with the shock formed at the separation shock-bow shock triple point. The surface heat transfer and pressure reach their highest values in the vicinity of the reattachment location.

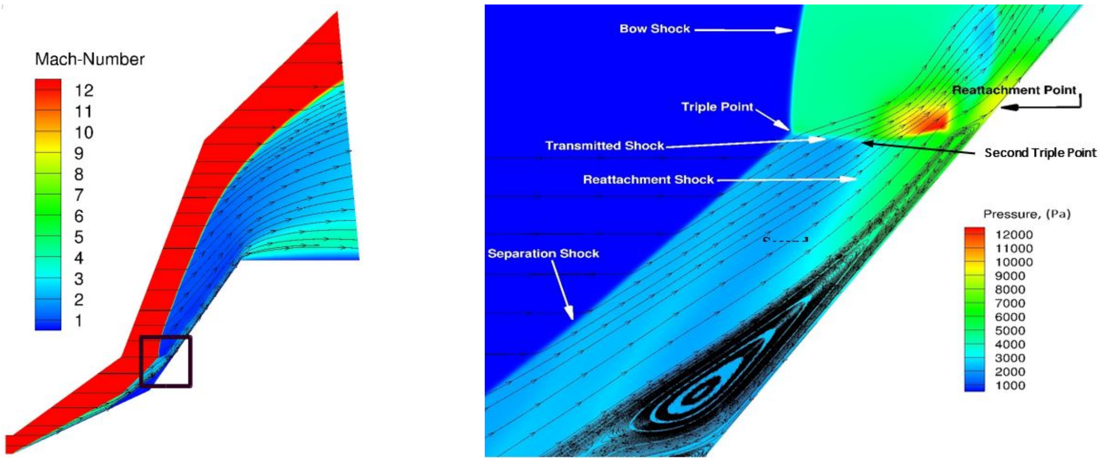

(a) Mach number (b) Static pressure

Figure 3: Flowfield structure for Run 1 (Youssefi and Knight [2017])

Run 1 (5.44 MJ/kg):

Fig. 4 displays the surface heat transfer and surface pressure for Run 1. Results are shown for the Perfect Gas and Park I models. The simulations were performed using GASPex and GASP, respectively. The Perfect Gas model displays closest agreement with experiment including an accurate prediction of the separation location. The spacing between experimental heat transfer and pressure transducers is significantly larger than the computational grid spacing, and therefore the actual experimental peak values of surface heat transfer and pressure may not have been recorded.

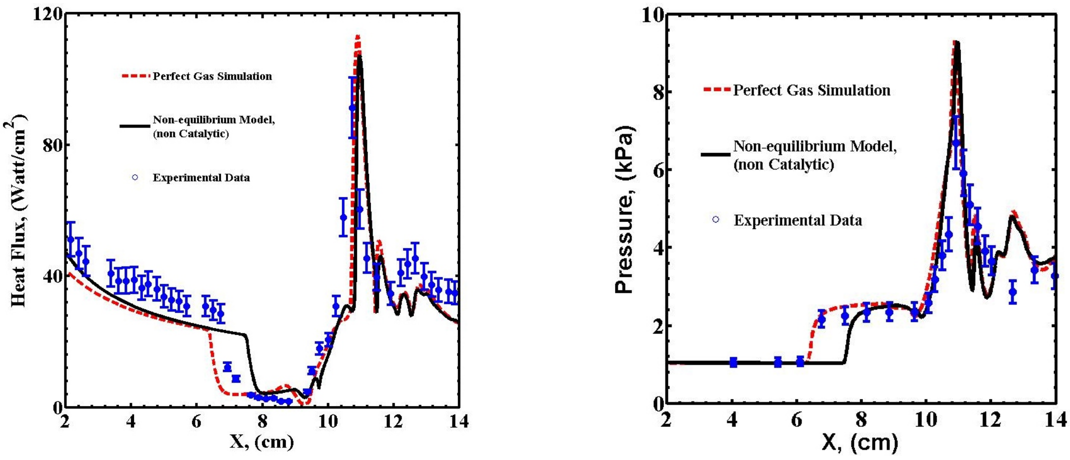

(a) Surface heat transfer

(b) Surface pressure

Figure 4: Surface heat transfer and pressure for Run 1 using Perfect Gas and Park I models (Youssefi and Knight [2017])

Run 2 (9.65 MJ/kg):

Fig. 5 shows the surface heat transfer and surface pressure for Run 2 using the Perfect Gas and Park I models. The simulations were performed using GASPex and GASP, respectively. The Perfect Gas model significantly overpredicts the size of the separation region, and consequently the location of the computed peak heat transfer and pressure is downstream of the experimental values. The Park I model shows closer agreement with experiment, although the separation location is farther downstream than in the experiment.

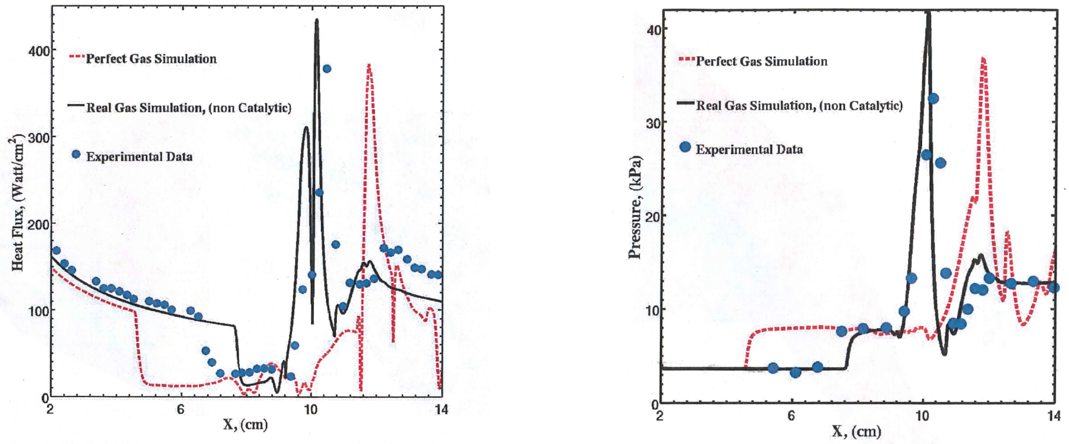

(a) Surface heat transfer

(b) Surface pressure

Figure 5: Surface heat transfer and pressure for Run 2 using Perfect Gas and Park I models (Youssefi and Knight [2016])

Fig. 6 presents the surface heat transfer and surface pressure for Run 2 using the Thermally Perfect, Nonreactive and Park I models. The simulations were performed using the code developed by Kianvashrad and Knight (Kianvashrad and Knight [2019]). The Thermally Perfect model accurately predicts the separation location, plateau pressure and recovery downstream of reattachment. As discussed above, the resolution of the experimental surface heat transfer and pressure transducers is significantly larger than the computational grid spacing in the vicinity of the peak values of heat transfer and pressure, and therefore the peak values may not have been resolved in the experiment. Similar to Fig. 5, the Park I and Nonreactive models predict a separation location further downstream than in the experiment.

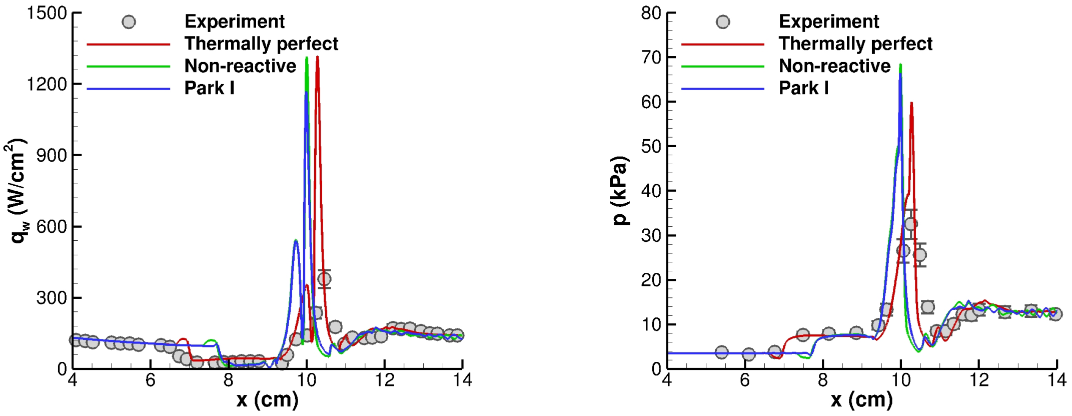

(a) Surface heat transfer

(b) Surface pressure

Figure 6: Surface heat transfer and pressure for Run 2 using Thermally Perfect, Nonreactive and Park I models (Kianvashrad and Knight [2019])

Run 6 (15.23 MJ/kg):

Fig. 7 displays the surface heat transfer and surface pressure for Run 6 using the Perfect Gas and Park I models. The simulations were performed using GASPex and GASP, respectively. The Perfect Gas model substantially overpredicts the size of the separation region, and consequently the location of the computed peak heat transfer and pressure is downstream of the experimental values. The Park I model shows closer agreement with experiment, although the separation location is farther downstream than in the experiment.

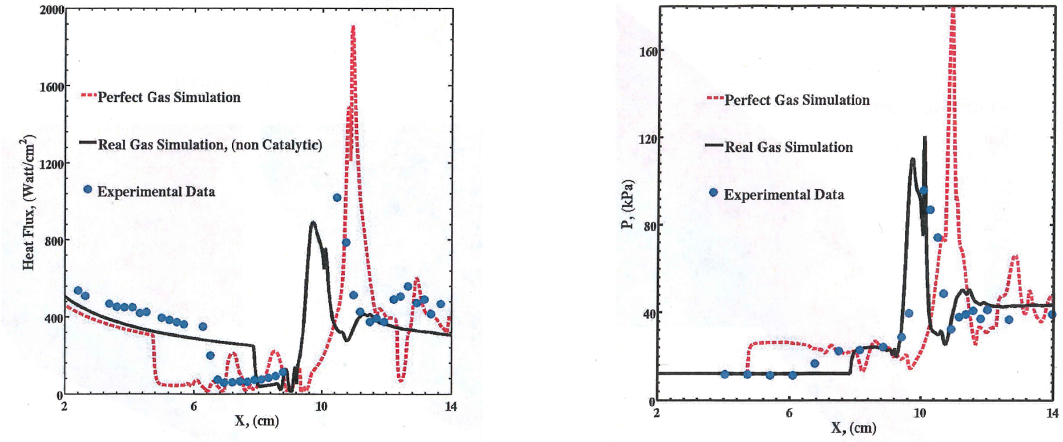

(a) Surface heat transfer

(b) Surface pressure

Figure 7: Surface heat transfer and pressure for Run 6 using Perfect Gas and Park I models (Youssefi and Knight [2016])

Run 4 (21.77 MJ/kg):

Fig. 8 displays the surface heat transfer and surface pressure for Run 4 using the Perfect Gas and Park I models. The simulations were performed using GASPex and GASP, respectively. Similar to Run Nos. 2 and 6, the Perfect Gas model substantially overpredicts the size of the separation region, and thus the location of the computed peak heat transfer and pressure is downstream of the experimental values. The Park I model shows close agreement with experiment.

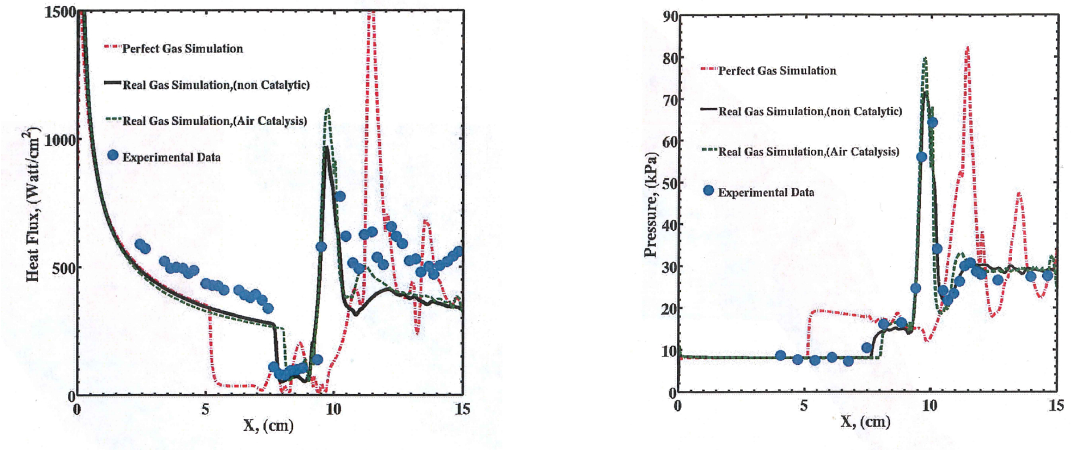

(a) Surface heat transfer

(b) Surface pressure

Figure 8: Surface heat transfer and pressure for Run 4 using Perfect Gas and Park I models (Youssefi and Knight [2016])

Fig. 9 presents the surface heat transfer and surface pressure for Run 4 using the Thermally Perfect, Nonreactive and Park I models. The simulations were performed using the code developed by Kianvashrad and Knight (Kianvashrad and Knight [2019]). Among the three models, the Thermally Perfect model displays the best prediction of the location of separation.

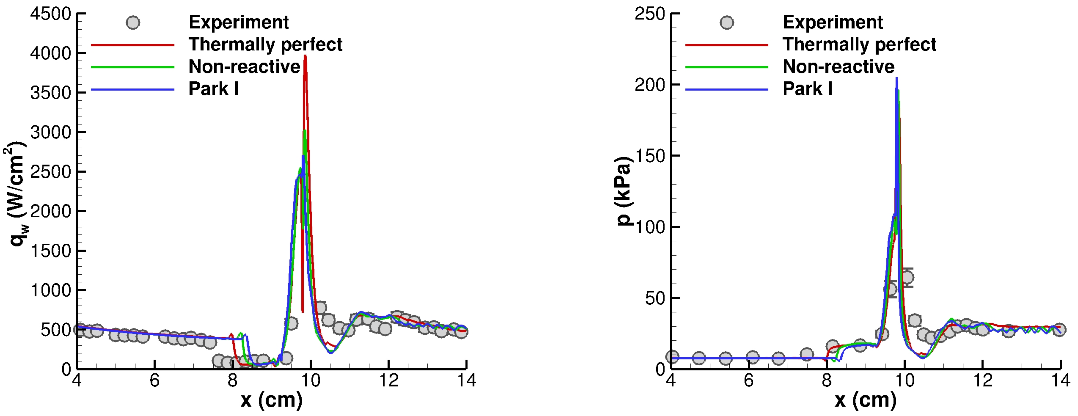

(a) Surface heat transfer

(b) Surface pressure

Figure 9: Surface heat transfer and pressure for Run 4 using Thermally Perfect, Nonreactive and Park I models (Kianvashrad and Knight [2019])

Hollow Cylinder Flare

The flowfield structure for the hollow cylinder flare is shown in Fig. 10. Mach contours of the entire flowfield (Fig. 10 (a)) and corner region (Fig. 10 (b)) are presented using the Perfect Gas model. The hollow cylinder generates a weak displacement thickness shock wave. The flare forms a conical shock which interacts with the laminar boundary layer on the cylinder. A separation shock forms and intersects with the flare shock to form a triple point. The reattachment shock intersects the resultant shock emanating from the triple point. The highest surface heat transfer and pressure occur in the vicinity of reattachment.

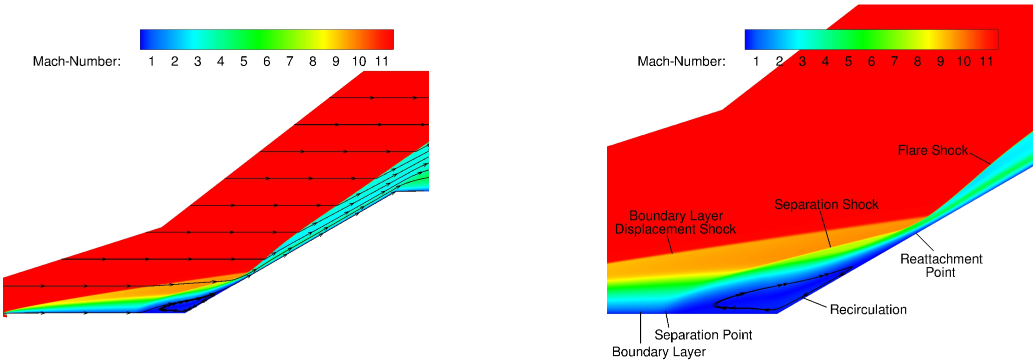

(a) Mach contours (b) Mach contours

Figure 10: Flowfield structure for Run 1 (Kianvashrad and Knight [2016])

Run 1 (5.07 MJ/kg) :

Fig. 11 shows the surface heat transfer and pressure for Run 1 using the Perfect Gas model. The simulation was performed using GASPex. The Perfect Gas model predicts a somewhat larger interaction reion than the experiment, with the peak surface pressure higher than in the experiment.

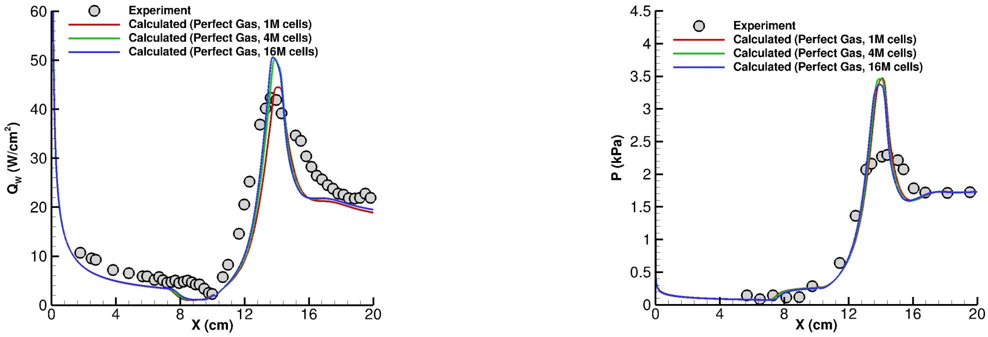

(a) Surface heat transfer (b) Surface pressure

Figure 11: Surface heat transfer and pressure for Run 1 using Perfect Gas model (Kianvashrad and Knight [2016])

Run 2 (10.43 MJ/kg):

Fig. 12 displays the surface heat transfer and pressure for Run 2 using the Perfect Gas and Park I models. The simulations were performed using GASPex and GASP, respectively. Also shown are results using two grids (Park I model) and three grids (Perfect Gas model) indicating grid converged solutions for both models. The Park I model shows a small separation region at the corner (Kianvashrad and Knight [2016]) while the Perfect Gas model displays no separation.

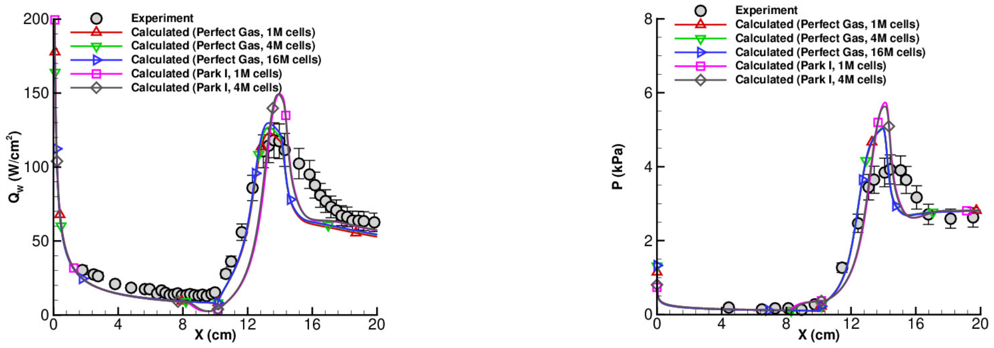

(a) Surface heat transfer (b) Surface pressure

Figure 12: Surface heat transfer and pressure for Run 2 using Perfect Gas and Park I models (Kianvashrad and Knight [2017a])

Fig. 13 shows the surface heat transfer and pressure for Run 2 using all four models. Closest agreement with experiment is achieved using the Thermally Perfect model. There is negligible difference between the Nonreactive and Park I model predictions.

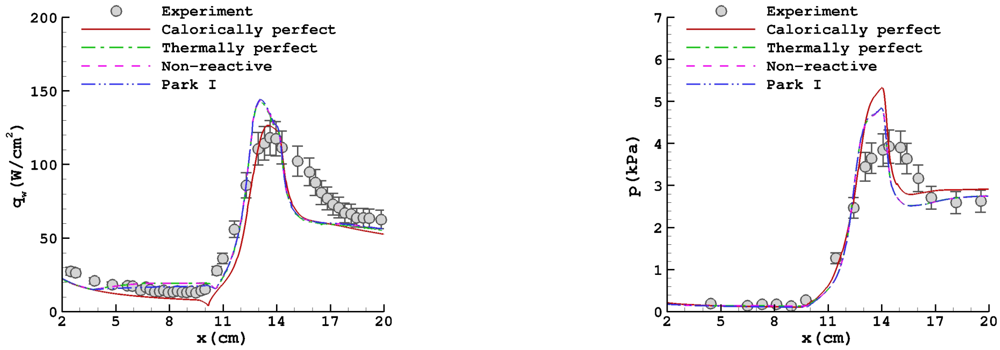

(a) Surface heat transfer (b) Surface pressure

Figure 13: Surface heat transfer and pressure for Run 2 using Perfect Gas ("Calorically perfect"), Thermally Perfect, Nonreactive and Park I models (Kianvashrad and Knight [2021])

Run 4 (15.54 MJ/kg):

Fig. 14 displays surface heat transfer and pressure for Run 4 using the Perfect Gas and Park I models. The simulations were performed using GASPex and GASP, respectively. Results using two grids (Park I model) and three grids (Perfect Gas model) are included. Both models predict a separation region with the Perfect Gas model the larger (Kianvashrad and Knight [2016]).

Run 5 (21.85 MJ/kg):

Fig. 15 shows the surface heat transfer and pressure for Run 5 using the Park I model with GASP. Fig. 16 displays the results for all four models using the code developed by Kianvashrad and Knight (Kianvashrad and Knight [2019]). Among the four models, the Thermally Perfect model displays the best prediction of the location of separation, and best overall agreement with experiment.

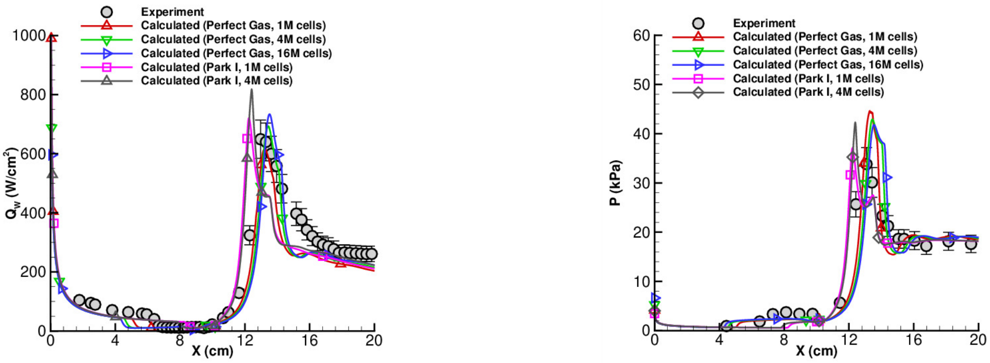

(a) Surface heat transfer

(b) Surface pressure

Figure 14: Surface heat transfer and pressure for Run 4 using Perfect Gas and Park I models (Kianvashrad and Knight [2017a])

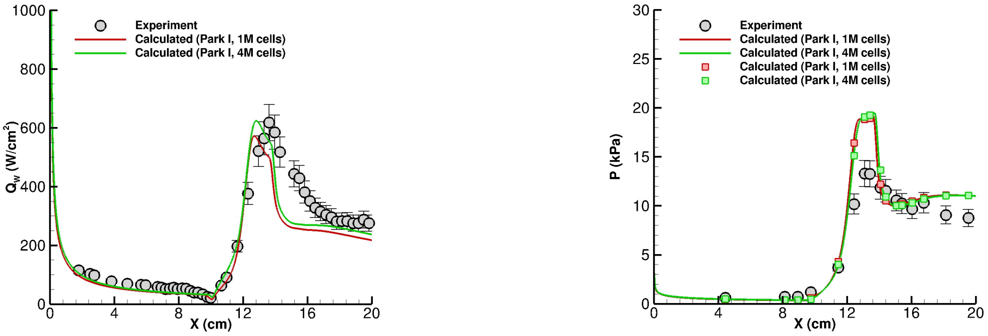

(a) Surface heat transfer

(b) Surface pressure

Figure 15: Surface heat transfer and pressure for Run 5 using Park I model (Kianvashrad and Knight [2017a])

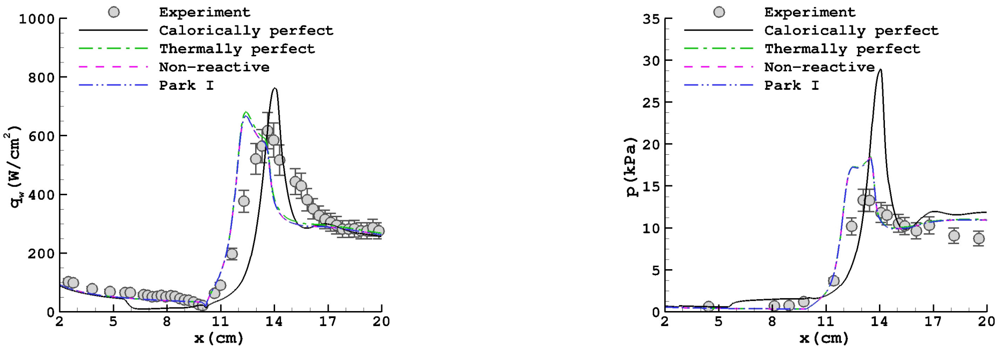

(a) Surface heat transfer

(b) Surface pressure

Figure 16: Surface heat transfer and pressure for Run 5 using Perfect Gas ("Calorically perfect"), Thermally Perfect, Nonreactive and Park I models (Kianvashrad and Knight [2021])

DISCUSSION

The results for the double cone and hollow cylinder flare indicate that the Thermally Perfect model provides best agreement with experiment. The Thermally Perfect model incorporates the temperature dependency of specific heats while otherwise assuming equilibrium flow (i.e., omits thermochemical reactions and vibrational-translational energy exchange). This result is indeed unexpected since the high stagnation enthalpies (up to 21 MJ/kg) would presumably cause significant thermochemical reactions and vibrational non-equilibrium.

The explanation to this apparent anomaly lies in the region of the flowfield where non-equilibrium effects occur and its relationship to the measured surface heat transfer and pressure. Figs. 17, 18 and 19 display mass fraction contours of NO, N and O for Run 4 of the double cone using the Park I model. This is the highest stagnation enthalpy for the double cone, and therefore it would be expected to exhibit the most significant non-equilibrium effects. Indeed, the region downstream of the triple point shows that virtually all of the molecular oxygen has been dissociated (Fig. 19). However, the reactions occur away from the boundary and downstream of the reattachment location, thereby not affecting the surface pressure and heat transfer within the interaction region. Fig. 20 shows the ratio $T_\alpha^{\rm vib}/T$ for N_2 and O_2 for Run 4 of the double cone using the Park I model. The translational-rotational temperature T and vibrational temperature $T_\alpha^{\rm vib}$ are very similar except within the region downstream of the triple point and away from the surface. Consequently, vibrational-translational energy exchange is unimportant for prediction of surface properties. A similar result holds for $T_\alpha^{\rm vib}$ for NO (Kianvashrad and Knight [2018]). Similar conclusions apply for the hollow cylinder flare.

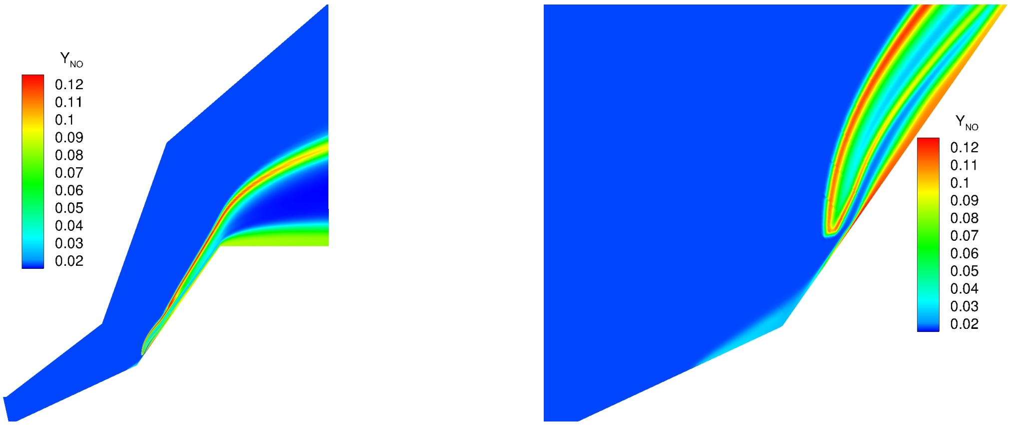

(a) Mass fraction of NO

(b) Mass fraction of NO (enlarged view)

Figure 17: Mass fraction contours of NO for Run 4 using Park I model (Kianvashrad and Knight [2018])

CONCLUSIONS

A series of hypersonic shock wave laminar boundary layer interaction experiments were simulated using four different models: Perfect Gas, Thermally Perfect, Nonreactive and Park I. These models incorporate increasing levels of physical complexity. The Perfect Gas model assumes constant specific heats and equilibrium flow. The Thermally Perfect model incorporates temperature dependent specific heats but retains the assumption of equilibrium flow. The Nonreactive and Park I models incorporate non-equilibrium effects of vibrational-translational energy exchange (Nonreactive and Park I models) and thermochemical reactions (Park I) models. The experiments were performed at the CALSPAN University of Buffalo Research Center (CUBRC) at stagnation enthalpies from 5.07 MJ/kg to 21.85 MJ/kg and Mach numbers from 10.9 to 13.2. Experimental diagnostics include surface heat transfer and pressure.

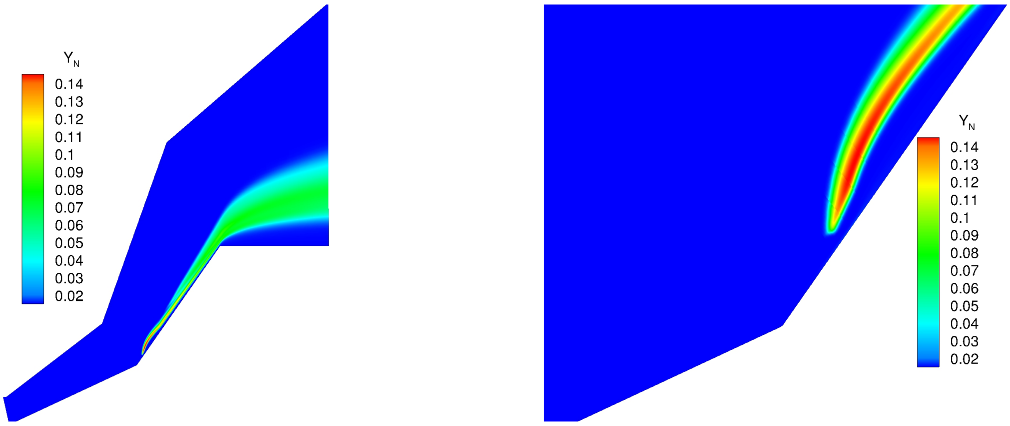

(a) Mass fraction of N (b) Mass fraction of N (enlarged view)

Figure 18: Mass fraction contours of N for Run 4 using Park I model (Kianvashrad and Knight [2018])

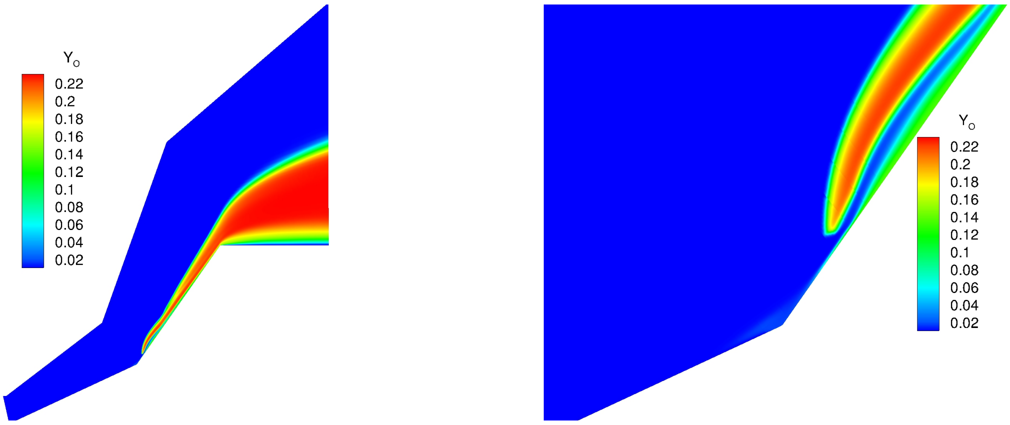

(a) Mass fraction of O (b) Mass fraction of O (enlarged view)

Figure 19: Mass fraction contours of N for Run 4 using Park I model (Kianvashrad and Knight [2018])

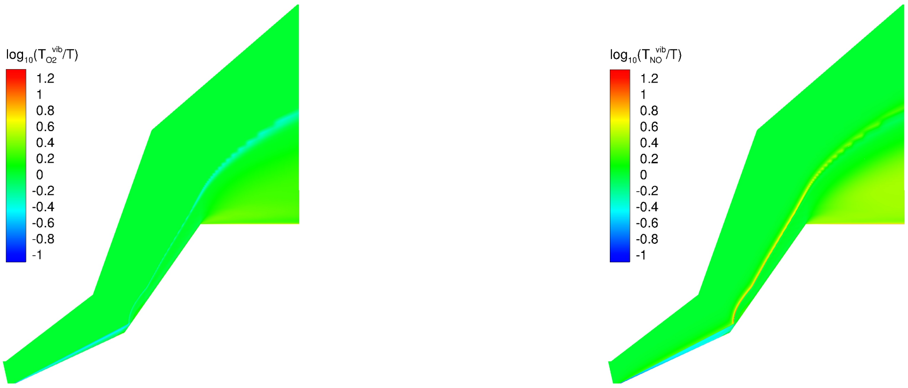

(a) N_2 (b) O_2

Figure 20: $\log_{10} T_\alpha^{\text{vib}}/T$ for N_2 and O_2 for Run 4 using Park I model

The Thermally Perfect model showed best agreement with experimental surface heat transfer and pressure. Incorporation of nonequilibrium effects in the Nonreactive and Park I model did not improve prediction and showed little difference with the Thermally Perfect model. The minimal effect of nonequilibrium physics on the surface heat transfer and pressure is explained by the flowfield structure. The region of non-equilibrium effects is downstream of the triple points generated by the shock-shock interaction and away from the boundary. Thus, the experimental data of surface heat transfer and pressure for the double cone and hollow cylinder flare configurations in this study do not constitute a stringest test of non-equilibrium effects in hypersonic shock wave laminar boundary layer interactions.

References

K Jackson, M Gruber, and S Buccellato. Mach 6-8+ Hydrocarbon-Fueled Scramjet Flight Experiment: The HIFiRE Flight 2 Project. *Journal of Propulsion and Power*, 31(1):36–53, January 2015. doi: 10.2514/1.B35350. URL `http://dx.doi.org/10.2514/1.B35350`.

B Perrett, B Sweetman, and M Fabey. US Navy Sees Chinese HGV as Part of Wider Threat. *Aviation Week and Space Technology*, January 2014. URL `http://aviationweek.com/awin/us-navy-sees-chinese-hgv-part-wider-threat`.

K Button. Making a Money Saver. *Aerospace America*, pages 16–19, June 2016.

J Longo. Present Results and Future Challenges of the DLR SHEFEX Program. AIAA Paper 2009-7226, American Institute of Aeronautics and Astronautics, October 2009. URL `http://dx.doi.org/10.2514/6.2009-7226`.

J Steelant, T Langener, F Di Matteo, K Hannemann, J Riehmer, M Kuhn, C Ditter, W Jung, M Marini, G Pezzella, M Cicala, and L Serre. Conceptual Design of the High-Speed Propelled Experimental Test Vehicle HEXAFLY. AIAA Paper 2015-3539, American Institute of Aeronautics and Astronautics, July 2015. URL `http://dx.doi.org/10.2514/6.2015-3539`.

G Pezzella, M Marini, B Reimann, and J Steelant. Aerodynamic Design Analysis of the HEXAFLY-INT Hypersonic Glider. AIAA Paper 2015-3644, American Institute of Aeronautics and Astronautics, July 2015. URL `http://dx.doi.org/10.2514/6.2015-3644`.

S Walker and F Rodgers. Falcon Hypersonic Technology Overview. AIAA Paper 2005-3253, American Institute of Aeronautics and Astronautics, May 2005. URL `http://dx.doi.org/10.2514/6.2005-3253`.

J Maus, B Griffith, and K Szema. Hypersonic Mach Number and Real Gas Effects on Space Shuttle Orbiter Aerodynamics. *Journal of Spacecraft and Rockets*, 21:136–141, 1984.

National Aeronautics and Space Administration. STS-1 Anomaly Report. Technical Report SSVEO IFA List Date 27 February 2003, OV-103, Columbia, 2003.

H Babinsky and J Harvey. *Shock Wave-Boundary-Layer Interactions*. Cambridge, New York, 2011.

D Knight and M Mortazavi. Simulation of Non-equilibrium Hypersonic Shock Wave Boundary Layer Interactions Using the Navier-Stokes Equations. CCD Report 2018-1, Rutgers University, 2018. coewww.rutgers.edu/knight.

M MacLean, M Holden, and A Dufrene. Comparison between CFD and Measurements for Real-Gas Effects on Laminar Shock Wave Boundary Layer Interaction, I. Oral Presentation, AIAA Aviation 2014, Atlanta, GA, 2014a.

M MacLean, M Holden, and A Dufrene. Comparison between CFD and Measurements for Real-Gas Effects on Laminar Shock Wave Boundary Layer Interaction, II. Oral Presentation, AIAA Aviation 2014, Atlanta, GA, 2014b.

A Dufrene, M MacLean, R Parker, T Wadhams, E Mundy, and M Holden. Charactérication of the New LENS Expansion Tunnel Facility. AIAA Paper 2010-1564, January 2010.

A Dufrene, M MacLean, R Parker, and M Holden. Experimental Characterization of the LENS Expansion Tunnel Facility including Blunt Body Surface Heating. AIAA Paper 2011-626, January 2011.

W Vincenti and C Kruger. Introduction to Physical Gas Dynamics. Krieger Publishing Company, Malabar, Florida, 1965.

R Millikan and D White. Systematics of Vibrational Relaxation. The Journal of Chemical Physics, 39 (12):3209–3213, 1963.

R Gupta, J Yos, R Thompson, and K Lee. A Review of Reaction Rates and Thermodynamic and Transport Properties for an 11-Species Air Model for Chemical and Thermal Nonequilibrium Calculations to 30000 K. Reference Report 1232, NASA, 1990.

C. Wilke. A Viscosity Equation for Gas Mixtures. Journal of Chemical Physics, 18(4):517–519, 1950.

C Park. On Convergence of Computation of Chemically Reacting Flow. AIAA Paper 1985-0247, January 1985.

R Neel and W McGrory. GASP and GASPex Version 5.1.2 Reference Guides. Aerosoft, Inc., Blacksburg, VA, 2014.

N Kianvashrad and D Knight. Simulation of hypersonic shock wave-laminar boundary layer interactions. In D Knight, M. Ivanov, and I. Lipatov, editors, *Progress in Flight Physics*, volume 9 of *EUCASS Book Series, Advances in Aerospace Sciences*, pages 165–176. European Conferece for Aeronautic and space Sciences, Torus Press.

M Rouhi Youseffi and D Knight. Assessment of CFD Capability for High Enthalpy Non-Equilibrium Flows with Strong Viscous-Inviscid Interaction. AIAA Paper 2015-0580, American Institute of Aeronautics and Astronautics, January 2015.

N Kianvashrad and D Knight. Simulation of Hypersonic Shock Wave Laminar Boundary Layer Interaction on Hollow Cylinder Flare. AIAA Paper 2016-0349, American Institute of Aeronautics and Astronautics, January 2016.

M Rouhi Youssefi and D Knight. Assessment of cfd capability for hypersonic shock wave boundary layer interactions, part ii. AIAA Paper 2016-0350, American Institute of Aeronautics and Astronautics, January 2016.

N Kianvashrad and D Knight. Simulation of Hypersonic Shock-Wave-Laminar-Boundary-Layer Interaction on Hollow Cylinder Flare. *AIAA Journal*, 55(1):322–326, January 2017a. doi: 10.2514/1.J055258. URL `http://dx.doi.org/10.2514/1.J055258`.

N Kianvashrad and D Knight. Simulation of Hypersonic Shock Wave Laminar Boundary Layer Interaction on Hollow Cylinder Flare, Part II. AIAA Paper 2017-3975, American Institute of Aeronautics and Astronautics, June 2017b. URL `https://doi.org/10.2514/6.2017-3975`.

N Kianvashrad and D Knight. Effect of Vibrational Temperature Boundary Condition of Isothermal Wall on Hypersonic Shock Wave Laminar Boundary Layer Interaction of a Hollow Cylinder Flare. EUCASS Paper 2017-97, European Conferece for Aeronautic and space Sciences, July 2017c. URL `https://doi.org/10.13009/EUCASS2017-97`.

M Rouhi Youssefi and D Knight. Assessment of cfd capability for hypersonic shock wave laminar boundary layer interactions. Aerospace, 4(2), April 2017. doi: doi:10.3390/aerospace4020025.

N Kianvashrad and D Knight. The Effect of Thermochemistry on Prediction of Aerothermodynamic Loading over a Double Cone in a Laminar Hypersonic Flow. AIAA Paper 2018-1812, American Institute of Aeronautics and Astronautics, January 2018.

D Knight and N Kianvashrad. Prediction of Aerothermodynamic Loading in Hypersonic Shock Wave Laminar Boundary Layer Interaction. Technical Report FP55-AERO2018-Knight, 3AF International Conference, March 2018.

N Kianvashrad and D Knight. Nonequilibrium Effects on Prediction of Aerothermodynamic Loading for a Double Cone. *AIAA Journal*, 57(7):2946–2963, July 2019. doi: 10.2514/1.J057883.

N Kianvashrad and D Knight. Effect of Thermodynamic Database and Non-Equilibrium on Hypersonic Flow Past Hollow Cylinder Flare. AIAA Journal, under review, 2021.

APPENDIX

Table 4: Thermochemistry Model Reactions

Reaction	C (m^3/kg·mole·s)	η	ϵ/k (K)	α	β	A_1	A_2	A_3	A_4	A_5
$N_2 + N_2 \rightarrow N + N + N_2$	$3.70 \cdot 10^{18}$	-1.6	113200	0.5	0.5	10.81	-12.61	0.683	-0.118	0.006
$N_2 + N \rightarrow N + N + N$	$1.11 \cdot 10^{19}$	-1.6	113200	0.5	0.5	10.81	-12.61	0.683	-0.118	0.006
$N_2 + NO \rightarrow N + N + NO$	$3.70 \cdot 10^{18}$	-1.6	113200	0.5	0.5	10.81	-12.61	0.683	-0.118	0.006
$N_2 + O_2 \rightarrow N + N + O_2$	$3.70 \cdot 10^{18}$	-1.6	113200	0.5	0.5	10.81	-12.61	0.683	-0.118	0.006
$N_2 + O \rightarrow N + N + O$	$1.11 \cdot 10^{19}$	-1.6	113200	0.5	0.5	10.81	-12.61	0.683	-0.118	0.006
$N_2 + O \rightarrow NO + N$	$3.18 \cdot 10^{10}$	0.1	37700	1.0	0.0	2.349	-4.828	0.455	-0.075	0.004
$O_2 + N_2 \rightarrow O + O + N_2$	$2.75 \cdot 10^{16}$	-1.0	59500	0.5	0.5	8.243	-4.127	-0.616	0.093	-0.005
$O_2 + N \rightarrow O + O + N$	$8.25 \cdot 10^{16}$	-1.0	59500	0.5	0.5	8.243	-4.127	-0.616	0.093	-0.005
$O_2 + NO \rightarrow O + O + NO$	$2.75 \cdot 10^{16}$	-1.0	59500	0.5	0.5	8.243	-4.127	-0.616	0.093	-0.005
$O_2 + O_2 \rightarrow O + O + O_2$	$2.75 \cdot 10^{16}$	-1.0	59500	0.5	0.5	8.243	-4.127	-0.616	0.093	-0.005
$O_2 + O \rightarrow O + O + O$	$8.25 \cdot 10^{16}$	-1.0	59500	0.5	0.5	8.243	-4.127	-0.616	0.093	-0.005
$NO + O \rightarrow N + O_2$	$2.16 \cdot 10^{5}$	1.29	19220	1.0	0.0	0.215	-3.657	0.843	-0.136	0.007
$NO + N_2 \rightarrow N + O + N_2$	$2.30 \cdot 10^{14}$	-0.5	75500	0.5	0.5	8.457	-7.784	0.228	-0.043	0.002
$NO + NO \rightarrow N + O + NO$	$2.30 \cdot 10^{14}$	-0.5	75500	0.5	0.5	8.457	-7.784	0.228	-0.043	0.002
$NO + O_2 \rightarrow N + O + O_2$	$2.30 \cdot 10^{14}$	-0.5	75500	0.5	0.5	8.457	-7.784	0.228	-0.043	0.002
$NO + N \rightarrow N + O + N$	$4.60 \cdot 10^{14}$	-0.5	75500	0.5	0.5	8.457	-7.784	0.228	-0.043	0.002
$NO + O \rightarrow N + O + O$	$4.60 \cdot 10^{14}$	-0.5	75500	0.5	0.5	8.457	-7.784	0.228	-0.043	0.002

NOTES

$k_f = C T_a^{\eta} e^{-\epsilon/kT_a}, \quad T_a = T^{\alpha} T_{\text{vib}}^{\beta}, \quad k_e = \exp\left(A_1 + A_2 z + A_3 z^2 + A_4 z^3 + A_5 z^4\right)$ where $z = 10^4/T$